

# The electronic properties of boron-doped germanium nanocrystals films

Dan Shan<sup>1,2</sup> · Menglong Wang<sup>2</sup> · Daoyuan Sun<sup>2</sup> · Yunqing Cao<sup>2</sup>

Received: 7 May 2023 / Accepted: 30 August 2023

Published online: 07 September 2023

© The Author(s) 2023 [OPEN](#)

## Abstract

Various doping concentrations of boron (B)-doped germanium nanocrystal (Ge NC) films were prepared using the plasma-enhanced chemical vapor deposition (PECVD) technique followed by thermal annealing treatment. The electronic properties of B-doped Ge NCs films combined with the microstructural characterization were investigated. It is worthwhile mentioning that the Hall mobilities  $\mu_{\text{Hall}}$  of Ge NCs films were enhanced after B doping and reached to the maximum of  $200 \text{ cm}^2 \text{ V}^{-1}$ , which could be ascribed to the reduction in surface defects states in the B-doped films. It is also important to highlight that the temperature-dependent mobilities  $\mu_{\text{H}}(T)$  exhibited different temperature dependence trends in the Ge NCs films before and after B doping. A comprehensive investigation was conducted to examine the distinct carrier transport properties in B-doped Ge NC films, and a detailed discussion was presented, focusing on the scattering mechanisms involved in the transport process.

**Keywords** Germanium nanocrystal · Electronic property · Temperature dependence Hall effect measurement · Scattering mechanism

## Abbreviations

Ge NCs	Germanium nanocrystals
PECVD	Plasma-enhanced chemical vapor deposition
a-Ge:H	Hydrogenated amorphous germanium
SCCM	Standard cubic centimeter per minute
XRD	X-ray diffraction
GBs	Grain boundaries
DBs	Dangling bonds

## Introduction

Over the past decade, there has been a growing interest in semiconductor nanocrystals based on Silicon and Germanium. These nanocrystals have gained attention due to their versatile applications in various devices, including light emitters, thin-film solar cells, photoelectric sensors, and nonvolatile memories [1–7]. Germanium, in particular, exhibits advantages such as larger electron and hole mobility, a narrower band-gap (0.67 eV), and high phonon responsivity in the near-infrared region

✉ Yunqing Cao, yqcao@yzu.edu.cn; Dan Shan, shandnju@126.com; Menglong Wang, wangml0708@126.com; Daoyuan Sun, sundaoyuan0808@126.com | <sup>1</sup>School of Information Engineering, Yangzhou Polytechnic Institute, Yangzhou 225127, China. <sup>2</sup>School of Physical Science and Technology/Microelectronics Industry Research Institute, Yangzhou University, Yangzhou 225009, China.



[8–10]. These properties make it suitable for the fabrication of Ge-based photodetectors and Ge-based thin film transistors (TFT) with superior device performance [7, 11–13]. However, achieving desired properties in Si and Ge NCs often necessitates active doping to enhance device performance [14–17]. Unfortunately, doping nanocrystals is challenging, and the process is further complicated by the phenomenon known as "self-purification". This phenomenon makes it difficult for defects or impurities to migrate toward the surface of a nanocrystal due to the small distances involved [18, 19]. Consequently, there has been limited research conducted on the electronic properties of doped Si or Ge NCs, highlighting the need for a deeper understanding of the fundamental carrier transport properties in these materials [20–24].

In our previous works, the electronic properties of P- and B-doped Si NCs films were investigated by the temperature-dependent Hall effect measurements [20–22]. Compared with B dopants, P impurities are more likely to substitutionally occupy the inner sites Si NCs. They can be easily electrically activated and provide a large number of charge carriers, which finally reduces the barriers height of grain boundaries (GBs) in the Si NCs films. Thus, it was reported that the scattering effect of grain boundaries could be suppressed by the introduction of P impurities in Si NCs films. In the present work, the microstructure and carrier transport properties of B-doped Ge NCs films have been investigated. It was found that the crystallization of Ge NCs films was degenerated when B impurities were introduced. Almost no significant increases of carrier concentrations were observed in Ge NCs films after B doping, indicating the doping efficiency of B is low in Ge NCs materials. Furthermore, carrier transport processes in Ge NCs films before and after B doping were systematically studied. There were different scattering mechanisms dominated the carrier transport process, respectively, in Ge NCs films with various doping concentrations. The possible microscopic mechanisms which to govern the charge transport were briefly discussed.

## Experiment

B-doped hydrogenated amorphous germanium (*a*-Ge:H) films were prepared by a plasma-enhanced chemical vapor deposition (PECVD) system using the gas mixtures of pure germane (GeH<sub>4</sub>, Nanjing, China), hydrogen (H<sub>2</sub>, Nanjing, China) and diborane (B<sub>2</sub>H<sub>6</sub>, 1% diluted in H<sub>2</sub>, Nanjing, China). The flow rate of GeH<sub>4</sub> was kept at 5 sccm (standard cubic centimeter per minute) during the growth process [20–22]. The boron concentrations were changed by adjusting the flow rate of B<sub>2</sub>H<sub>6</sub> ( $F_B$ ), which controlled at 0 sccm (un-doped), 0.5, 1 and 3 sccm, respectively. The gas-chamber pressure, substrate temperature and radio frequency power were 10 m Torr, 250 °C and 30 W, respectively. The thickness of all samples is designed to be 150 nm. After deposition, all the samples were subsequently annealed in a conventional furnace at temperatures of 500 °C for 1 h in nitrogen ambient for crystallization. Quartz plates and monocrystalline Si wafers were selected as substrates for the various measurements [20–22].

The microstructures of all films were characterized using Raman spectroscopy (HR800, Jobin Yvon Horiba Inc.) and X-ray diffraction (MXP-III, Bruker Inc.). The optical band-gap of the films was determined by analyzing the optical absorption spectra obtained from a Shimadzu UV-3600 spectrophotometer using Tauc plots. The electronic properties, including dark conductivity, Hall mobility, and carrier concentration, were determined through temperature-dependent Hall measurements using a variable temperature Hall effect measurement system (model: LakeShore 8400 series, LakeShore). The measurements were conducted in a standard van der Pauw (VDP) configuration with an electromagnet generating a magnetic induction of 0.6 T. The temperature range for the Hall measurements was from 300 to 650 K. To achieve ohmic contacts, all samples were prepared with coplanar Al electrodes at the four corners using vacuum thermal evaporation, followed by a 30-min alloying treatment at 400 °C.

## Results and discussion

### Microstructure characterization

Raman spectroscopy, commonly employed to investigate the microstructures of annealed nanocrystalline films, was conducted using an Ar<sup>+</sup> laser with a wavelength of 514 nm as the excitation light source. Figure 1 displays the Raman spectra of B-doped Ge NC films with different doping concentrations. A weak and broad Raman band centered at 273 cm<sup>-1</sup> is observed in the as-deposited film, which is indicative of the transverse-optical (TO) vibration mode of amorphous Ge–Ge bonds. Conversely, in the samples subjected to the annealing procedure, a sharp peak emerges near 300 cm<sup>-1</sup>, indicating the formation of Ge NCs phases [23, 25]. The volume fraction of crystalline  $X_C$  can be estimated as the formula:  $X_C = \frac{I_c}{I_c + \sigma I_a}$  [26]. To analyze the Raman spectra, a deconvolution process was employed, separating the spec-

trum into two Gaussian components representing nanocrystalline (*nc-Ge*) and amorphous (*a-Ge*) phases. The deconvolution results are depicted in the inset of Fig. 1. The integrated intensities of the crystalline and amorphous peaks are represented by  $I_c$  and  $I_a$ , respectively. In our analysis, a value of  $\sigma$  equal to 0.88 was used, signifying the ratio of the integrated Raman cross sections between the crystalline and amorphous phases. It can be calculated that  $X_C$  is about 86% for the un-doped Ge NCs film and was gradually decreased to nearly 65% for B-doped Ge NCs film with the maximum doping amount of  $F_B = 3$  sccm. Similar results in Si NCs films had been reported at our preliminary work [27]. The reduction in  $X_C$  was primarily attributed to the introduction of dopants, resulting in increased fluctuations in bond angles and bond lengths as the dopants were incorporated into the films. This phenomenon led to the degradation of the short-range order. From the aforementioned discussion, we can conclude that the incorporation of B dopants results in reduced crystallization within the Ge NCs films.

The microstructure of B-doped Ge NCs films with various doping concentrations was further investigated by XRD measurement. The XRD patterns of all samples deposited on quartz substrates are shown in Fig. 2. It was clearly observed that the diffraction peak at near  $2\theta = 27^\circ$  and  $45^\circ$ , which associated with the poly-crystalline planes of (111) and (220) for Ge, respectively, appeared in all the films [28]. Moreover, the diffraction peak corresponding to the (111) plane in Ge NCs films exhibits a slight reduction in intensity following B doping. This suggests that the proportion of crystalline material in the films may have decreased as a result of B doping [29]. This observation implies that the introduction of B dopants can adversely affect the quality of Ge NCs, leading to a decrease in crystallization within the Ge NCs films. These findings are consistent with the results obtained from the Raman analysis.

The optical band-gap  $E_g$  is commonly determined using Tauc plots, where  $(\alpha h\nu)^{1/2} = B(h\nu - E_g)$ . Here,  $\alpha$  represents the absorption coefficient,  $h\nu$  is the photon energy, and  $B$  is a constant. This method is employed to characterize the light absorption in nanocrystalline semiconductor films [30, 31]. Figure 3 shows the Tauc's plot of  $(\alpha h\nu)^{1/2}$  versus photon energy  $h\nu$  for B-doped Ge NCs films. It is found that the value of optical band-gap, which was reported as 1.6 eV for the un-doped Ge NCs film in our previous work [32], was slightly reduced to 1.5 eV for the B-doped Ge NCs with  $F_B = 0.5$  sccm and dropped to 1.2 eV when the B doping concentration increased to  $F_B = 3$  sccm. The optical band-gap is known to be influenced by the presence of disordered grain boundary regions in the crystallized sample, which typically exhibit a higher optical band-gap compared to the nanocrystalline regions [33]. The widespread distribution of grain boundary regions in Ge NC films contributes significantly to the overall optical band-gap. Therefore, the decrease in optical band-gap for the B-doped Ge NCs films may be ascribed to the decline of nanocrystalline components caused by the introduction of B dopants that have already been described in the above.

## Room temperature Hall effect measurement

In order to gain a deeper understanding of the electronic properties in B-doped Ge NCs films at different doping concentrations, Hall effect measurements were employed, which was utilized to provide enhanced insights into the behavior of carriers in the Ge NCs films. In Fig. 4a, room temperature carrier concentrations for Ge NCs films before and after B

**Fig. 1** the Raman spectrum of Ge NCs films with various B doping concentrations. The inset is the Gauss decomposition of Raman peak

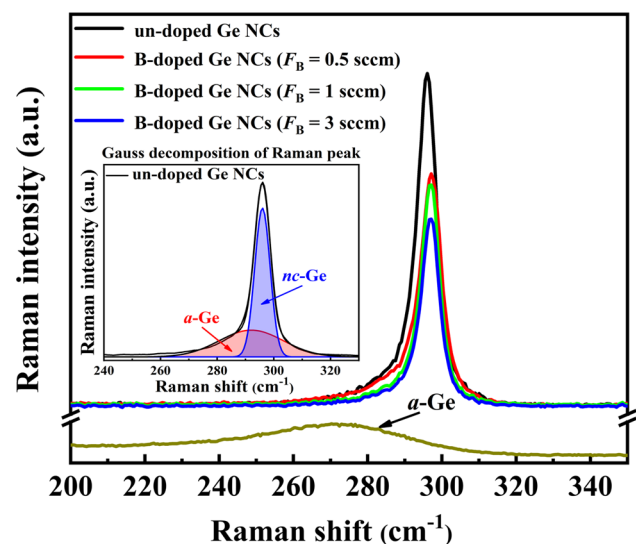


**Fig. 2** The XRD patterns of Ge NCs films with various B doping concentrations

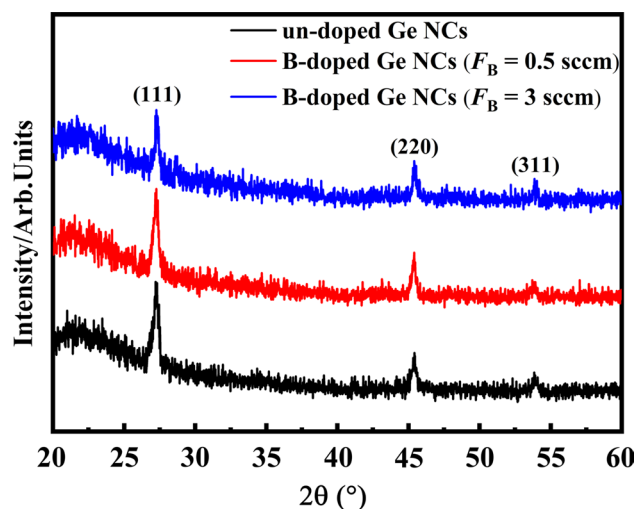
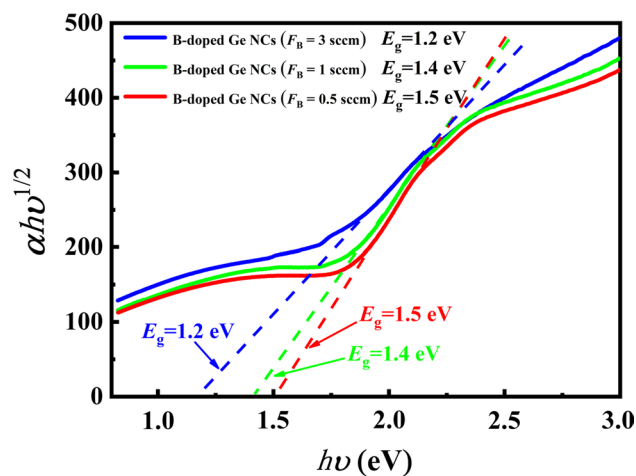


**Fig. 3** the Tauc's plot of  $(\alpha h\nu)^{1/2}$  versus photon energy  $h\nu$  for Ge NCs films with various B doping concentrations



doping are presented. It was interesting to find that the carrier concentration of un-doped Ge NCs film was nearly reached to  $10^{18} \text{ cm}^{-3}$  order with a p-type behavior. It was reported that the presence of a significant hole concentration in Ge NCs film, even without deliberate doping, can be attributed to the existence of deep-acceptor-like surface states. These surface states, often associated with dangling bonds (DBs), result in the accumulation of numerous negative charges at the surfaces [32]. As a result, the energy bands in the vicinity of the surface exhibit an upward bending, thereby attracting additional holes within the film. Consequently, the un-doped Ge NCs film experiences a pronounced increase in hole concentration. However, the hole concentration was barely increased in Ge NCs films after B doping as if the dopants could not enter into the Ge NCs. As we know, the dopants may have difficulty entering the core of nanocrystalline Si or Ge according to the so-called self-purification effect, especially the Si or Ge NCs with small sizes [18, 34]. Therefore, there is no more activated impurities that can contribute to the carrier concentration in the B-doped Ge NCs films.

Furthermore, the Hall mobilities  $\mu_{\text{Hall}}$  in B-doped Ge NCs films were also investigated at room temperature as shown in Fig. 4b. The Hall mobility is about  $182 \text{ cm}^2 \text{ V}^{-1}$  in Ge NCs film before doping, exhibiting a normal electrical performance compared with other reports [32]. After doping, it is very interesting to find that the value of  $\mu_{\text{Hall}}$  is higher than that of the un-doped sample. The Hall mobility was firstly enhanced and reached to nearly  $200 \text{ cm}^2 \text{ V}^{-1}$  for B-doped Ge NCs film with  $F_B = 1 \text{ sccm}$ , then decreased with increasing the B doping concentration. As we are aware, the carrier mobility in bulk Si is typically reduced as the doping concentration increases, primarily due to the strong scattering effect caused by impurities. However, the situation is quite different in the case of B-doped Ge NCs, where we observe an enhanced Hall mobility. This unconventional behavior can be attributed to several factors which will be examined in detail.

The relatively low carrier mobility observed in poly-crystalline and nanocrystalline Si or Ge is typically attributed to two primary factors: strong scattering at grain boundaries and the presence of defect states, which encompass the crystalline

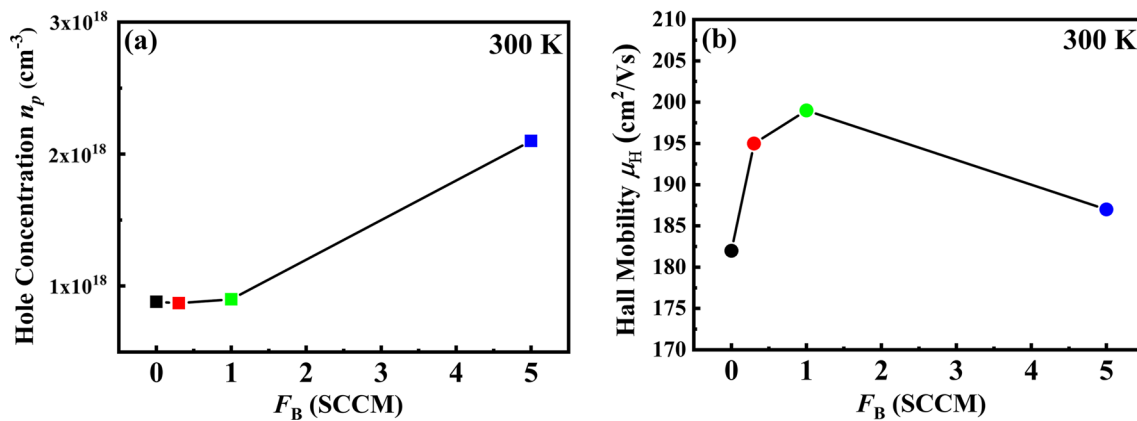


**Fig. 4** **a** Room temperature carrier concentrations and **b** Room temperature Hall mobilities for Ge NCs films before and after B doping

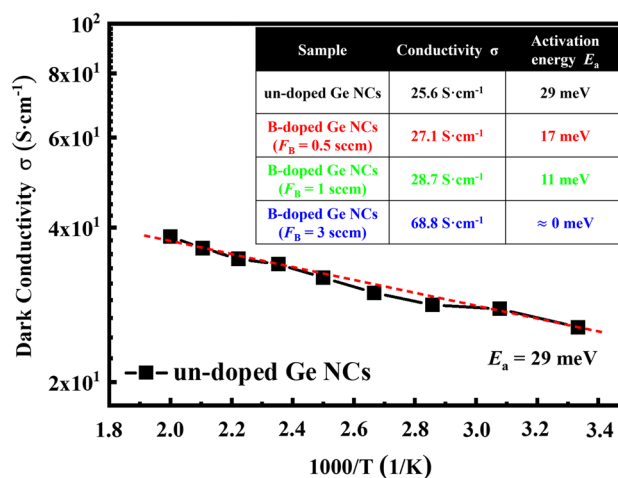
quality and interface defect states. Notably, the dangling bonds play a significant role in this regard, as they have the ability to trap carriers and generate a depletion region that subsequently affects carrier mobility [35–37]. However, the surface defect states can be well-passivated by the dopants. In our previous research, we investigated the effects of phosphorus (P) doping in Si NCs and made a significant discovery. We found that the introduction of P impurities effectively passivated the dangling bonds within the Si NCs. This passivation process played a crucial role in enhancing the electron mobility within the P-doped Si NCs, as we documented in our previous study [21]. In contrast to phosphorus impurities, boron impurities exhibit a distinct preference for occupying surface sites on nanocrystals rather than settling within the core of the nanocrystals. Hong et al. made an additional observation regarding the behavior of B atoms in Si NC films. They found that B atoms initially substituted the inactive threefold Si atoms present in the defect states of the Si NC films. Subsequently, these B atoms replaced the fourfold Si atoms, leading to electrically active doping [38]. Based on the preceding discussion, it becomes evident that B dopants, which occupy the surface sites, effectively passivate the defect states. Therefore, the observed enhancement in Hall mobility following B doping can be attributed to the reduction in surface defect states in our current study.

### Temperature-dependent Hall effect measurement

To gain a deeper understanding of the transport properties of B-doped Ge NC films, particularly regarding the scattering mechanisms involved in the transport process, we conducted an investigation of temperature-dependent Hall effects, which covered a temperature range spanning from 300 to 650 K. As shown in Fig. 5, temperature-dependent dark conductivity for un-doped Ge NCs film was measured at the temperature from 300 to 500 K. It was clearly found that the sample exhibited a linear relationship of the  $\ln\sigma$  versus  $T^{-1}$  plot, which indicates that carrier transport within the Ge NCs film is primarily governed by thermal activation conduction [29]. The activation energy,  $E_a$ , representing the energy difference between the Fermi level and the top of the valence band in p-type semiconductors, can be determined by analyzing the slope of  $\ln\sigma$  versus  $T^{-1}$  curve according to the Arrhenius plots  $\sigma = \sigma_0 \exp(-E_a/k_B T)$ . The deduced activation energy  $E_a$  of the un-doped Ge NCs films is only about 29 meV and gradually decreased to nearly 0 meV after B doping with a series of doping concentration (insert of Fig. 5). Compared with the band-gap of 1.6 eV for the un-doped Ge NCs film, the relatively small activation energies observed in all the Ge NC films can be attributed primarily to the presence of deep-acceptor-like surface states. As mentioned earlier, these surface states lead to the accumulation of holes and cause the Fermi level to be pinned near the top of the valence band.

To extract information about the scattering mechanisms in the transport process, temperature-dependent Hall mobilities were investigated at the temperature range from 300 to 650 K. As can be seen from Fig. 6, it should be pointed out that the curves of temperature dependence Hall mobilities have different trends for Ge NCs films before and after B doping, which implies different scattering mechanisms in these samples. For the un-doped Ge NCs film, the mobility is firstly increased with increasing the temperature to near about 450 K and then, decreased with further increasing the temperature. Considerable research efforts have been devoted to the increased Hall mobility with temperature in the previous works including our reports [22, 39, 40]. It can be interpreted that the carrier transport process is mainly dominated by the grain boundaries scattering in un-doped Ge NCs film at room temperature. The grain boundaries,

**Fig. 5** temperature-dependent dark conductivity for un-doped Ge NCs film; the insert are the deduced activation energy  $E_a$  for Ge NCs films with various B doping concentrations



characterized by a higher concentration of defects, tend to trap charged carriers to a greater extent than the interior of the grains. As a result, band bending occurs at the grain boundaries, impeding carrier transport. However, as the temperature increases, the carriers gain additional energy, facilitating easier traversal of the potential barriers at the grain boundaries. Consequently, the mobility exhibits an increase with temperature, attributed to the reduced scattering caused by the grain boundaries [39].

However, the mobilities exhibited different temperature dependence trends after B doping, especially in the temperature region 300–450 K. It can be found that the Hall mobility decreases monotonously with the temperature in the whole measurement temperature range, which implies that the grain boundaries scattering may not dominate the carrier transport process in B-doped Ge NCs films. We suggested it can be ascribed to the reduction in crystallization in Ge NCs films after B doping. The lower crystallization in Ge NCs films, the fewer and smaller grains spreading over the films that due to the decrease in grain boundaries. Thus, the grain boundaries scattering mechanism could not play an important role in the carrier transport process in B-doped Ge NCs films. To further explore the scattering mechanism in B-doped Ge NCs films, Fig. 7 plots the  $\log \mu_H$  as a function of  $\log T$  in the temperature range from 300 to 650 K. The  $\mu_H(T)$  can be described by the following equation  $\mu_H(T) \propto T^n$ . It can be estimated that the data yield  $n = -0.8$  for the B-doped Ge NCs film with  $F_B = 0.5$  sccm and  $n = -0.2$  for the B-doped Ge NCs film with  $F_B = 3$  sccm. It is generally believed that typical scattering is acoustic phonons, ionized and neutral impurities scattering, which yield values of  $-1.5$ ,  $1.5$  and  $0$ , respectively [41]. However, in our present works, the B dopants are more likely to occupy the surface sites of Ge NCs dots than be ionized to realize electrically active doping. Therefore, the exponents, which show the  $n$ -value of about  $-0.2$  and  $-0.8$ , indicate that the carrier transport is dominated by a superposition of acoustic phonon scattering, neutral impurities scattering as well as grain boundaries scattering [42]. It must also be mentioned that the grain boundaries scattering is weaker in the B-doped Ge NCs film with  $F_B = 3$  sccm than in the film with  $F_B = 0.5$  sccm. Consequently, the  $n$ -value of  $-0.8$  for the

**Fig. 6** The temperature dependence Hall mobilities of Ge NCs films with various B doping concentrations

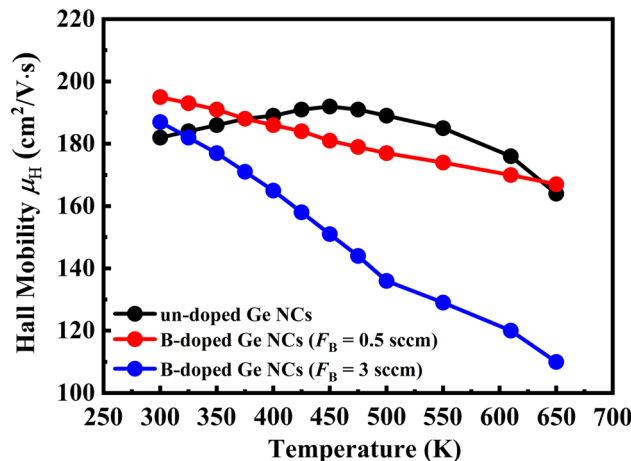
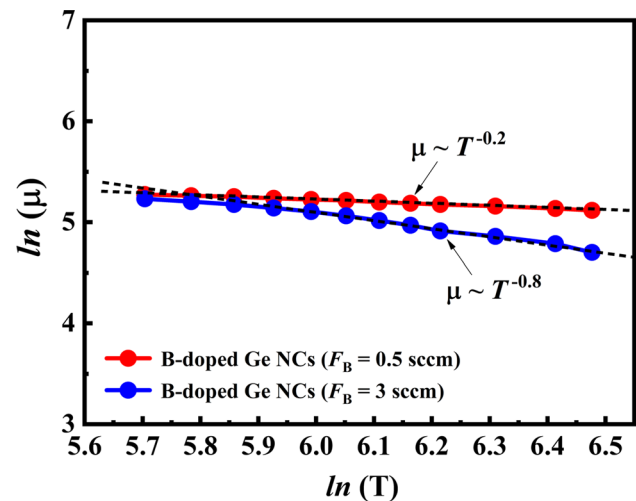


**Fig. 7** The  $\log \mu_H$  as a function of  $\log T$  for the B-doped Ge NCs film with  $F_B = 0.5$  and 3 sccm in the temperature range from 300 to 650 K



B-doped Ge NCs film with  $F_B = 3$  is shown closer to  $-1.5$ , which indicates the acoustic phonon scattering should play a more and more important role in the Ge NCs films after B doping.

## Conclusion

In summary, B-doped Ge NCs films with various doping concentrations were fabricated by thermal annealing of the corresponding  $\alpha$ -Ge:H films. Both the crystallinity and average grain size in Ge NCs films were gradually decreased with increasing B doping concentrations. A high hole concentration could be achieved to more than  $10^{18} \text{ cm}^{-3}$  order due to the holes accumulation caused by the acceptor-like surface states in Ge NCs film. However, the hole concentrations in Ge NCs films after B doping had barely increased, which implies that the B atoms hardly enter into the core of Ge NCs to realize electrically active doping. Another interesting finding is that the Hall mobilities in Ge NCs films were unusually increased after B doping, which can be ascribed to the reduction in surface defects states well-passivated by the dopants. Based on the temperature-dependent Hall effect measurement, the scattering mechanisms during carrier transport process in Ge NCs films were investigated. It can be found that different scattering mechanisms were observed in the Ge NCs films before and after B doping. In un-doped Ge NCs film, the grain boundaries scattering mainly dominated the carrier transport process. After B doping, the carrier transport process was dominated by a superposition of acoustic phonon scattering, neutral impurities scattering and grain boundaries scattering and the acoustic phonon scattering played a more and more important role when further increasing the B doping concentration.

**Author contributions** DS and YC conceived the idea and carried out the experiments. MW and DS participated in the preparation of the samples. DS, MW, and YC took part in the experiments and the discussion of the results. DS and YC drafted the manuscript. All authors reviewed the manuscript.

**Funding** This work was supported by Major project of Natural Science Foundation of Education Department in Jiangsu Province (22KJA510008), Science and Technology Planning Project of Yangzhou City (YZ2022209 and YZ2021132), Innovation technology platform project (YZ2020268) jointly built by Yangzhou City and Yangzhou University, "Qing Lan Project" of Young and Middle-aged Academic Leaders in Jiangsu Province (2020), Jiangsu new perception technology and intelligent scene Application Engineering Research Center (2021) and Jiangsu Province vocational education wisdom scene application "double teacher" master teacher studio (2021).

**Availability of data and materials** The data used to support the findings of this study are available from the corresponding authors upon request.

## Declarations

**Competing interests** The authors declare no conflict of interest.

**Open Access** This article is licensed under a Creative Commons Attribution 4.0 International License, which permits use, sharing, adaptation, distribution and reproduction in any medium or format, as long as you give appropriate credit to the original author(s) and the source, provide a link to the Creative Commons licence, and indicate if changes were made. The images or other third party material in this article are included in the article's Creative Commons licence, unless indicated otherwise in a credit line to the material. If material is not included in the article's Creative Commons licence and your intended use is not permitted by statutory regulation or exceeds the permitted use, you will need to obtain permission directly from the copyright holder. To view a copy of this licence, visit <http://creativecommons.org/licenses/by/4.0/>.

## References

1. Morozova S, Alikina M, Vinogradov A, Pagliaro M. Silicon quantum dots: synthesis, encapsulation, and application in light-emitting diodes. *Front Chem*. 2020. <https://doi.org/10.3389/fchem.2020.00191>.
2. Madani HH, Shayesteh MR, Reza M. A carbon nanotube (CNT)-based SiGe thin film solar cell structure. *J Optoelectron Nanostruct Winter*. 2021; 6(1).
3. Wang B, Tang L, Zhang Y, Teng KS. Research progress in the preparation of black silicon and its photoelectric detection. In 2021 International Conference on Optical Instruments and Technology: IRMMW-THz Technologies and Applications. SPIE, 2022; <https://doi.org/10.1117/12.2620633>
4. Zhou Z, Shen T, Wang P, Guo Q, Wang Q, Ma C, Xin K, Zhao K, Yu Y, Qin B, Liu YY, Yang J, Hong H, Liu K, Liu C, Deng HX, Wei Z. Low symmetric sub-wavelength array enhanced lensless polarization-sensitivity photodetector of germanium selenium. *Sci Bull*. 2023. <https://doi.org/10.1016/j.scib.2023.01.013>.
5. Lim D, Son J, Cho K, Kim S. Quasi-nonvolatile silicon memory device. *Adv Mater Technol*. 2020. <https://doi.org/10.1002/admt.20200091>.
6. Chou YC, Tsai CW, Yi CY, Chung WH, Wang SY, Chien CH. Neuro-inspired-in-memory computing using charge-trapping memtransistor on germanium as synaptic device. *IEEE Trans Electron Devices*. 2020. <https://doi.org/10.1109/TED.2020.3008887>.
7. Lin YW, Sun CJ, Chang HH, Huang YH, Yu TY, Wu YC, Hou FJ. Self-induced ferroelectric 2-nm-thick Ge-doped HfO<sub>2</sub> thin film applied to Ge nanowire ferroelectric gate-all-around field-effect transistor. *Appl Phys Lett*. 2020. <https://doi.org/10.1063/5.0029628>.
8. Ashburn P, Bagnall D (2006) Silicon–germanium: properties, growth and applications. In Springer handbook of electronic and photonic materials, pp 481–498
9. Cariou R, Tang J, Ramay N, Ruggeri R, Cabarrocas PR. Low temperature epitaxial growth of SiGe absorber for thin film heterojunction solar cells. *Sol Energy Mater Sol Cells*. 2015. <https://doi.org/10.1016/j.solmat.2014.11.018>.
10. Dey A, Das D. Narrow band gap high conducting nc-Si1-xGex: H absorber layers for tandem structure nc-Si solar cells. *J Alloys Compd*. 2019. <https://doi.org/10.1016/j.jallcom.2019.07.320>.
11. Zhang N, Shao J, Hao Y, Chen Y, Zhang Z, Zhang Y, Gao L, Miao T, Zhong Z, Hu H, Wang L. Photoresponse enhancement in Ge MSM photodetector with Ge micropillar array. *IEEE Trans Electron Devices*. 2023. <https://doi.org/10.1109/TED.2022.3231805>.
12. Zhou D, Chen G, Fu S, Zuo Y, Yu Y. Germanium photodetector with distributed absorption regions. *Opt Express*. 2020. <https://doi.org/10.1364/OE.390079>.
13. Jang K, Kim Y, Park J, Yi J. Electrical and structural characteristics of excimer laser-crystallized polycrystalline Si<sub>1-x</sub>Ge<sub>x</sub> thin-film transistors. *Materials*. 2019. <https://doi.org/10.3390/ma12111739>.
14. Fan X, Zhang Z, Zhu J, Yuan K, Zhou J, Zhang X, Tang D. Systematic investigations on doping dependent thermal transport properties of single crystal silicon by time-domain thermoreflectance measurements. *Int J Therm Sci*. 2022. <https://doi.org/10.1016/j.ijthermalsci.2022.107558>.
15. Li D, Chen J, Xue Z, Sun T, Han J, Chen W, Talbot E, Demoulin R, Li W, Xu J, Chen K. Atomic-scale study on the dopant distribution in phosphorus and boron-doped Si nanocrystals/SiO<sub>2</sub> multilayers. *Appl Surf Sci*. 2023. <https://doi.org/10.1016/j.apsusc.2022.155260>.
16. Liu W, Shi J, Zhang L, Han A, Huang S, Li X, Peng J, Yang Y, Gao Y, Yu J, Jiang K, Yang X, Li Z, Zhao W, Du J, Song X, Yin J, Wang J, Yu Y, Shi Q, Ma Z, Zhang H, Ling J, Xu L, Liu Z. Light-induced activation of boron doping in hydrogenated amorphous silicon for over 25% efficiency silicon solar cells. *Nat Energy*. 2022. <https://doi.org/10.1038/s41560-022-01018-5>.
17. Jeong H, Kim YS, Baik S, Kang H, Jang J, Kwon H. High and uniform phosphorus doping in germanium through a modified plasma assisted delta doping process with H<sub>2</sub> plasma treatment. *IEEE Electron Device Lett*. 2022. <https://doi.org/10.1109/LED.2022.3182730>.
18. Dalpian GM, Chelikowsky JR. Self-purification in semiconductor nanocrystals. *Phys Rev Lett*. 2006. <https://doi.org/10.1103/PhysRevLett.96.226802>.
19. Chelikowsky JR. The role of self-purification and the electronic structure of magnetically doped semiconductor nanocrystals. *Phase Trans*. 2006. <https://doi.org/10.1080/01411590601030100>.
20. Shan D, Qian M, Ji Y, Jiang X, Xu J, Chen K. The change of electronic transport behaviors by P and B doping in nano-crystalline silicon films with very high conductivities. *Nanomaterials-Basel*. 2016. <https://doi.org/10.3390/nano6120233>.
21. Shan D, Ji Y, Li D, Xu J, Qian M, Xu L, Chen K. Enhanced carrier mobility in Si nano-crystals via nanoscale phosphorus doping. *Appl Surf Sci*. 2017. <https://doi.org/10.1016/j.apsusc.2017.07.011>.
22. Shan D, Cao Y, Yang R, Wang H, Tao T. The carrier transport properties of B-doped Si nanocrystal films with various doping concentrations. *J Nanomater*. 2020. <https://doi.org/10.1155/2020/3698543>.
23. Caldelas P, Rolo AG, Gomes MJM, Alves E, Ramos AR, Conde O, Yerci S, Turan R. Raman and XRD studies of Ge nanocrystals in alumina films grown by RF-magnetron sputtering. *Vacuum*. 2008. <https://doi.org/10.1016/j.vacuum.2008.03.067>.
24. Imajo T, Ishiyama T, Saitoh N, Yoshizawa N, Suemasu T, Toko K. Record-high hole mobility germanium on flexible plastic with controlled interfacial reaction. *ACS Appl Electron Mater*. 2021. <https://doi.org/10.1021/acsaelm.1c00997>.

25. Hao Z, Kochubei SA, Popov AA, Volodin VA. On Raman scattering cross section ratio of amorphous to nanocrystalline germanium. *Solid State Commun.* 2020. <https://doi.org/10.1016/j.ssc.2020.113897>.
26. Tsu R, Gonzalez J, Chao SS, Lee SC, Tanaka K. Critical volume fraction of crystallinity for conductivity percolation in phosphorus-doped Si: F: H alloys. *Appl Phys Lett.* 1982. <https://doi.org/10.1063/1.93133>.
27. Song C, Wang X, Huang R, Song J, Guo YQ. Effects of doping concentration on the microstructural and optoelectrical properties of boron doped amorphous and nanocrystalline silicon films. *Mater Chem Phys.* 2013. <https://doi.org/10.1016/j.matchemphys.2013.07.017>.
28. Park MI, Kim CS, Park CO, Jeoung SC. XRD studies on the femtosecond laser ablated single-crystal germanium in air. *Opt Lasers Eng.* 2005. <https://doi.org/10.1016/j.optlaseng.2004.12.010>.
29. Shan D, Ji Y, Xu J, Lu P, Jiang X, Xu J, Chen K. Microstructure and carrier-transport behaviors of nanocrystalline silicon thin films annealed at various temperatures. *Phys Status Solidi A.* 2016. <https://doi.org/10.1002/pssa.201532864>.
30. Hao XJ, Cho EC, Flynn C, Shen YS, Conibeer G, Green MA. Effects of boron doping on the structural and optical properties of silicon nanocrystals in a silicon dioxide matrix. *Nanotechnology.* 2008. <https://doi.org/10.1088/0957-4484/19/42/424019>.
31. Mirabella S, Agosta R, Franzò G, Crupi I, Miritello M, Lo Savio R, Di Stefano MA, Di Marco S, Simone F, Terrasi A. Light absorption in silicon quantum dots embedded in silica. *J Appl Phys.* 2009. <https://doi.org/10.1063/1.3259430>.
32. Shan D, Wang H, Tang M, Xu J. Microscopic understanding of the carrier transport process in Ge nanocrystals films. *J Nanomater.* 2018. <https://doi.org/10.1155/2018/2685210>.
33. Das D, Bhattacharya K. Characterization of the Si: H network during transformation from amorphous to micro- and nanocrystalline structures. *J Appl Phys.* 2006. <https://doi.org/10.1063/1.2384812>.
34. Ni Z, Zhou S, Zhao S, Peng W, Yang D, Pi X. Silicon nanocrystals: unfading silicon materials for optoelectronics. *Adv Mater Sci Eng.* 2019. <https://doi.org/10.1016/j.msere.2019.06.001>.
35. Seager CH, Castner TG. Zero-bias resistance of grain boundaries in neutron-transmutation-doped polycrystalline silicon. *J Appl Phys.* 1978. <https://doi.org/10.1063/1.325394>.
36. Hellmich W, Müller G, Krötz G, Derst G, Kalbitzer S. Optical absorption and electronic transport in ion-implantation-doped polycrystalline SiC films. *Appl Phys A.* 1995. <https://doi.org/10.1007/BF01538389>.
37. Seto JYW. The electrical properties of polycrystalline silicon films. *J Appl Phys.* 1975. <https://doi.org/10.1063/1.321593>.
38. Hong SH, Kim YS, Lee W, Kim YH, Song JY, Jang JS, Park JH, Choi S, Kim KJ. Active doping of B in silicon nanostructures and development of a Si quantum dot solar cell. *Nanotechnology.* 2011. <https://doi.org/10.1088/0957-4484/22/42/425203>.
39. Myong SY, Lim KS, Konagai M. Effect of hydrogen dilution on carrier transport in hydrogenated boron-doped nanocrystalline silicon-silicon carbide alloys. *Appl Phys Lett.* 2006. <https://doi.org/10.1063/1.2037871>.
40. Shan D, Tong G, Cao Y, Tang M, Xu J, Yu L, Chen K. The effect of decomposed  $PbI_2$  on microscopic mechanisms of scattering in  $CH_3NH_3PbI_3$  films. *Nanoscale Res Lett.* 2019. <https://doi.org/10.1186/s11671-019-3022-y>.
41. Sze SM, Li Y, Ng KK. *Physics of semiconductor devices.* New York: Wiley; 2021.
42. Kittel C. *Introduction to solid state physics, vol. 7.* New York: Wiley; 1996.

**Publisher's Note** Springer Nature remains neutral with regard to jurisdictional claims in published maps and institutional affiliations.